RAA 2019 Vol. 19 No. 1, 9(8pp) doi: 10.1088/1674–4527/19/1/9

http://www.raa-journal.org *http://iopscience.iop.org/raa*

Research in Astronomy and Astrophysics

Ancient subsurface structure beneath crater Clavius: constraint by recent high-precision gravity and topography data

Zhen Zhong[1,2,3], Jian-Guo Yan[2,1*] and J. Alexis P. Rodriguez[4]

[1] School of Physics and Electronic Science, Guizhou Normal University, Guiyang 550001, China
[2] State Key Laboratory of Information Engineering in Surveying, Mapping and Remote Sensing, Wuhan University, Wuhan 430079, China; *jgyan@whu.edu.cn*
[3] Guizhou Provincial Key Laboratory of Radio Astronomy and Data Processing, Guizhou Normal University, Guiyang 550025, China
[4] Planetary Science Institute, 1700 East Fort Lowell Road, Suite 106, Tucson, AZ 85719-2395, USA

Received 2018 May 8; accepted 2018 July 7

Abstract With the increasing precision of the GRAIL gravity field models and topography from LOLA, it is possible to investigate the substructure beneath crater Clavius. An admittance between gravity and topography data is commonly used to estimate selenophysical parameters, including load ratio, crustal thickness and density, and elastic thickness. Not only a surface load, but also a subsurface load is considered in estimation. The algorithm of particle swarm optimization (PSO) with a swarm size of 400 is employed as well. Results indicate that the observed admittance is best-fitted by the modeled admittance based on a spherical shell model, which was proved to be unsatisfactory in the previous study. The best-fitted load ratio f is around -0.194. Such a small load ratio conforms to the direct proportion between the nearly uncompensated topography and its corresponding negative gravity anomaly. It also indicates that a surface load dominates all the loads. Constrained within $2\sigma_{\rm STD}$, a small crustal thickness ($\sim$30 km) and a crustal density of $\sim$2587 kg m^{-3} are found, quite close to the results from previous GRAIL research. Considering the well constrained crustal thickness and density, the best-fitted elastic thickness ($\sim$7 km) is rational. This result is slightly smaller than the previous study ($\sim$12 km). Such difference can be attributed to the difference in crustal density used and the precision of gravity and topography data. Considering that the small difference between the modeled gravity anomaly and observations is quite small, a parameter inversed here could be an indicator of the subsurface structure beneath Clavius.

Key words: Moon — planetary systems: planets and satellites: fundamental parameters — planetary systems methods: data analysis

1 INTRODUCTION

Lunar gravity anomalies are mainly caused by surface topography and density variations at the crust-mantle interface. Analogously to the Earth's lithosphere, the lunar lithosphere can adjust to loads acting on it and such a response is generated as the bending of the lithosphere. Then the bending can produce density variations at the crust-mantel interface, finally generating a gravity anomaly. Hence, the free-air gravity anomaly and surface topography are commonly used to probe the possible subsurface structure referring to crustal thickness $b_{\rm c}$ and density $\rho_{\rm c}$, and effective elastic thickness $T_{\rm e}$. The elastic thickness is an indicator of the lithospherical strength and is an important factor to constrain ancient lunar thermal evolution as well (Huang et al. 2014; Wieczorek et al. 2013). Academically, a statistical admittance between gravity anomaly and topography is generally employed to investigate the parameters mentioned above.

Considering the non-negligible membrane stresses that support loads (Turcotte et al. 1981; Zhong & Zuber

* Corresponding author.

2000), the lunar lithosphere is supposed to be modeled as a thin elastic spherical shell. Owing to its nonlinearity, it is complicated to directly solve its governing equation of the shell. However, it will be possible to resolve such an equation when the estimated parameters are presumed to be isotropic within studied areas. Then the relations between loads and bending of the lithosphere can be expanded in the spherical harmonic domain (McGovern et al. 2002; Crosby & McKenzie 2005; Belleguic et al. 2005; Huang & Wieczorek 2012; Beuthe et al. 2012). Not only do loads act on the surface, but also in the subsurface. Forsyth (1985) introduces load ratio f between subsurface and surface loads to consider both cases. Such consideration plays an important role in the global best-fit when estimating parameters (Forsyth 1985; McGovern et al. 2002; Zhong et al. 2014, 2018).

The crater Clavius is located in the rugged southern highlands of the Moon, centered at (58.4° S, 14.4° W) and with a radius of $\sim$113 km. This crater is one of the oldest formations on the lunar surface. It is relatively well-preserved from the Nectarian period. Crosby & McKenzie (2005) firstly investigated the elastic thickness over crater Clavius, using the low-precision line of sight accelerations from *Lunar Prospector*. The Gravity Recovery and Interior Laboratory (GRAIL) gravity field models show an unprecedented high-precision over the last five years. The updated GRAIL model even expands to a degree and order of 1500 (Park et al. 2015). In practice, the maximum degree of the gravity field model and topography is truncated to no more than 200, since the deflection of the crustal-mantle interface in responses to loads makes only a negligible contribution to the observed gravity anomaly beyond degree and order 150 (Wieczorek et al. 2013).

In this paper, the lunar lithosphere is considered as a thin elastic shell. A localized spectral admittance analysis is performed between GRAIL gravity field model GL0990D (Konopliv et al. 2014) and LOLA topography (Smith et al. 2010). The modeled admittance spectra are interpreted according to loading models including surface and subsurface loads. The particle swarm optimization (PSO) (Shi 1998; Kennedy & Eberhart 2001) algorithm is also employed to estimate selenophysical parameters including load ratio f, crustal thickness b_c and density ρ_c, and elastic thickness T_e. The best-constrained parameters over crater Clavius will provide a new insight into the ancient subsurface structure during the Nectarian period.

2 METHODS

2.1 Statistical Admittance between Gravity and Topography

The gravity g and topography h on a reference sphere can be given as a linear combination of spherical harmonics as (Wieczorek & Simons 2005, 2013)

$$g(\Omega) = \sum_{ilm} g_{lm} Y_{lm}(\Omega) \ , \quad h(\Omega) = \sum_{ilm} h_{lm} Y_{lm}(\Omega) \ , \tag{1}$$

where Y_{lm} denotes a spherical harmonic of degree l and order m, while g_{lm} and h_{lm} are the spherical harmonic expansion coefficients of g and h, respectively. Ω represents the position on the sphere referring to colatitude θ and longitude φ. i ranges from 1 to 2 for $\cos(m\varphi)$ and $\sin(m\varphi)$. In order to investigate selenophysical parameters at a localized region within angular radius θ_0, the global distributed gravity and topography are supposed to be localized by an axisymmetric windowing function $\psi(\theta_0)$ up to maximum degree l_win (Wieczorek & Simons 2005, 2013)

$$C_{ilm} = \frac{4\pi\Delta\rho R^3}{M(2l+1)} \sum_{n=1}^{l+3} \frac{{}^n h_{ilm}}{R^n n!} \frac{\Pi_{j=1}^n (l+4-j)}{l+3} \ , \tag{2}$$

where $C_{ilm} = C_{ilm}^1 + C_{ilm}^2 + \left(1 - \frac{b_c}{R}\right)^l C_{ilm}^3 + \left(1 - \frac{z_b}{R}\right)^l \left(C_{ilm}^4 + C_{ilm}^5\right)$ is the normalized Legendre polynomial of degree j. The localized gravity and topography are $g(\Omega)\psi(\theta_0)$ and $h(\Omega)\psi(\theta_0)$, respectively. The total cross-power $S_{\Phi\Gamma}(l)$ of the localized gravity and topography is expressed by

$$\begin{aligned} \sum_{l=0}^{\infty} S_{\Phi\Gamma}(l) &= \sum_{l=0}^{\infty} \sum_{m=-l}^{l} \Phi_{lm}\Gamma_{lm} \\ &= \frac{1}{4\pi} \int_{\Omega} \left[\psi(\theta_0)\, g(\Omega)\right] \left[\psi(\theta_0)\, h(\Omega)\right] d\Omega \ . \end{aligned} \tag{3}$$

Similarly, we can get the auto-power spectrum $S_{\Phi\Phi}(l)$ and $S_{\Gamma\Gamma}(l)$ of the localized gravity and topography, respectively. The wavelength-dependent localized admittance $z(l)$ and correlation $\gamma(l)$ can be given by

$$z(l) = \frac{S_{\Phi\Gamma}(l)}{S_{\Gamma\Gamma}(l)} \ , \quad \gamma(l) = \frac{S_{\Phi\Gamma}(l)}{\sqrt{S_{\Phi\Phi}(l) S_{\Gamma\Gamma}(l)}} \ . \tag{4}$$

The localized admittance error is estimated as (Bendat & Piersol 2000; Wieczorek & Simons 2013)

$$\sigma_z^2(l) = \frac{S_{\Gamma\Gamma}(l)}{S_{\Phi\Phi}(l)} \frac{1-\gamma^2(l)}{2l} \ . \tag{5}$$

2.2 Misfit Function

Given a series of parameters such as ρ_c, f, b_c and T_e, the modeled gravity can be deduced from the governing equation of a thin spherical shell. Using Equations (2)–(5), we can calculate the modeled admittance. If the measurement errors follow a Gaussian distribution, these aforesaid parameters can be estimated by minimizing the misfit between the modeled admittance and the observations. The misfit function is generally replaced by the chi-squared function (Belleguic et al. 2005)

$$\sigma^2 = \frac{1}{N} \sum_{l=l_{\mathrm{win}}}^{l_{\max}} \left[\frac{z^{\mathrm{obs}}(l) - z^{\mathrm{mod}}(l)}{\sigma_z(l)} \right]^2 , \tag{6}$$

where $z^{\mathrm{obs}}(l)$ and $z^{\mathrm{mod}}(l)$ are the observed and modeled admittances for a given degree l in terms of Equation (4) respectively, $\sigma_z(l)$ is the error of the observed admittance shown in Equation (5), l_{win} is the maximum degree of the windowing function shown in Equation (2) and $l_{\max}$ is the maximum degree of the utilized gravity. N is the number of degrees of freedom (which equals $l_{\max} - 2l_{\mathrm{win}} - 4$ in this study). The standard deviation of the chi-squared function is approximately equal to $\sqrt{2/N}$. The global best-fitted values of the parameters can be constrained within $2\sigma_{\mathrm{STD}} = 2\sqrt{2/N}$.

2.3 Modeled Gravity Anomaly

In order to minimize the misfit function in Equation (6), calculating the gravity anomaly in the modeled admittance is firstly needed. Given a series of parameters (f, b_c, ρ_c and T_e), the subsurface density variation can be deduced, especially at the crust-mantle interface. The resultant gravity anomaly arising at a density-contrast interface can be calculated according to the finite-amplitude correction from Wieczorek & Phillips (1998), which is as follows

$$C_{ilm}^{+} = \frac{4\pi\Delta\rho R^3}{M(2l+1)} \sum_{n=1}^{l+3} \frac{{}^{n}h_{ilm}}{R^n n!} \frac{\prod_{j=1}^{n}(l+4-j)}{l+3} , \tag{7}$$

where M is the mass of the Moon, $\Delta\rho$ is the density contrast at the density variation interface, while i ranges from 1 to 2 for cos($m\varphi$) and sin($m\varphi$). Other parameters are given in Table 1.

The modeled gravity anomalies are summed at four interfaces in our model. These interfaces include surface, crust-mantle interface, subsurface load and its reference interface. These interfaces are summarized in Table 2. The potential coefficients at every interface are estimated according to Equation (7). All the coefficients are sums of the coefficients for the four interfaces

$$\begin{aligned} C_{ilm} =& C_{ilm}^{1} + \left(\frac{R-b_c}{R}\right)^l C_{ilm}^{2} \\ &+ \left(\frac{R-z_b}{R}\right)^l \left(C_{ilm}^{3} + C_{ilm}^{4}\right) , \end{aligned} \tag{8}$$

where z_b is the depth of subsurface load and we take a depth equivalent to crustal thickness in this study ($z_b = b_c$). Then the modeled gravity anomalies at reference radius r are given by

$$\Delta g = \frac{GM}{r^2} \sum_{ilm} \left(\frac{R}{r}\right)^2 (l+1)\, C_{ilm} Y_{ilm}(\Omega) , \tag{9}$$

where G is the gravitational constant. The coefficients of the modeled gravity anomalies are $(l+1)C_{ilm}$, which are used in calculation of the modeled admittance according to Equation (4).

3 RESULTS AND DISCUSSION

The GRAIL gravity field model GL0990D (Konopliv et al. 2014) and topography data from LOLA (Smith et al. 2010) are considered in our admittance analysis. The gravity and topography data can be expressed to degrees and orders of 990 and 2050, respectively. Considering the fact that the deflection of the lithosphere in response to loads makes only a negligible contribution beyond spherical harmonic degree and order 150, these gravity and topography data are truncated up to 200 (corresponding to maximum degree $l_{\max} = 200$). The studied area is constrained within an angular radius of 5°, corresponding to a spherical harmonic bandwidth of 52. Then, the number of degrees of freedom considered in this analysis is 88, with a corresponding $2\sigma_{\mathrm{STD}}$ of 0.2998. It means that the parameters are constrained with a root mean square (RMS) misfit σ lower than 1.2998. Topography (Fig. 1a) and free-air gravity anomaly (Fig. 1b) around crater Calvius (circled in black) are shown in Figure 1. The low-lying craters demonstrate a direct proportion in the form of a negative gravity anomaly, while ridges around craters exhibit a small positive gravity anomaly. Most of the areas around Clavius show a nearly isostatic state.

In order to estimate parameters describing crater Clavius, we use a nonlinear algorithm, PSO, to minimize the misfit σ between the modeled admittance and observations. We apply a swarm size of 400 and 50 iterations in PSO to inverse the parameters. The best-fitted crustal thickness and density are close to 30 km and 2587 kg m^{-3}, respectively. A small load ratio f of –0.194 is found. The elastic thickness is constrained around 7 km. The spectra

Table 1 Nominal Parameter Values

Parameter name	Value or range
Load ratio f	$-0.8 \sim 5$
Mean crustal density ρ_c(kg m^{-3})	2000$\sim$3200
Mean crustal thickness b_c (km)	0.0$\sim$60
Lithospheric elastic thickness T_e (km)	0.0$\sim$150
Surface gravity acceleration g (m s^{-2})	1.721
Reference radius R (km)	1737.15
Mass of the Moon M (kg)	$7.3458998185 \times 10^{22}$
Poisson's ratio of lithosphere ν	0.25
Young's modulus of lithosphere E (Pa)	1.0×10^{12} (McGovern et al. 2002)
Mantle density ρ_m(kg m^{-3})	3220 (Wieczorek et al. 2013)

Table 2 The Reference Interfaces Employed in Modeled Gravity Anomaly Calculation

No.	Interface	Height of Interface	Density contrast	Reference radius
1	Surface	h	ρ_c	R
2	Crust-Mantle interface	–$(h_\mathrm{b} + w_\mathrm{t})$	$\rho_\mathrm{m}\rho_\mathrm{c}$	Rb_c
3	Subsurface load	$w_\mathrm{b}w_\mathrm{t}$	ρ_b	Rz_b
4	Reference layer of Subsurface load	–$(h_\mathrm{b} + w_\mathrm{t})$	–ρ_b	Rz_b

of modeled admittance and observation in Figure 2 climb until degree 60. Then, they descend slowly until almost degree 75. The spectra ascend after that degree, but they decline again after degree 80. Such declines stop until degree 123; then the spectra rise again until degree 135. It is evident that the modeled admittance spectrum shows a similar fluctuation with the observed spectrum. The corresponding misfit σ is close to 1.2491. Meanwhile, the spectrum of correlation is almost close to unity except for deviation around degree 75.

In order to test the acceptable ranges of the best-fitted parameters within the $2\sigma_\mathrm{STD}$ constraint, we have carried out a trade-off study in Figure 3 and an analysis of the exact range of parameters in Figure 4. In the trade-off study between T_e and f in Figure 3(a), the best-fitted elastic thickness T_e ranges from 2 km to 8 km, with a corresponding load ratio f between –0.235 and –0.197. The other panels in Figure 3 exhibit a small value of T_e in the range [6.5 km, 7.5 km]. The best-fitted crustal thickness falls in the range [27.5 km, 31 km] and crustal density varies between 2577 kg m^{-3} and 2597 kg m^{-3}. Moreover, the misfit σ in Figure 3(a) is quite a bit lower than those in the other panels. This result indicates that the load ratio f is sensitive to elastic thickness T_e, rather than b_c and ρ_c. Such lowest misfit σ is coincident with the corresponding large ranges of T_e and f.

To further find an exact range of parameters, Figure 4(a) and Figure 4(b) give a load ratio f of $-0.194^{+0.0094}_{-0.0036}$ and a crustal thickness of $29^{+1.5}_{-1.2}$ km, respectively. Such a small load ratio coincides with that in Figure 3(a), which indicates that a surface load dominates all the loads. Such a small value of f is also coincident with the direct proportion between surface low-lying topography and negative gravity anomaly in Figure 1. The other panels in Figure 4 exhibit a best-fitted crustal density varying between 2580 kg m^{-3} and 2590 kg m^{-3}, and a best-estimated elastic thickness ranging from 6.62 km to 7.25 km. In the research of Wieczorek et al. (2013), the estimated crustal thickness and density around Clavius are around 31 km and 2600 kg m^{-3}, respectively. It is evident that the best-inversed crustal thickness ($\sim$30 km) and density ($\sim$2587 kg m^{-3}) in our study are quite close to the results of Wieczorek et al. (2013).

The previous research of Crosby & McKenzie (2005) found that a spherical shell loading model is less satisfactory for Clavius. Based on a thin plate model with a two-layer crust, and an assumption with an upper crustal density of 2900 kg m^{-3} and a lower density of 3000 kg m^{-3}, they estimated an elastic thickness of $\sim$12 km. However, our research indicates that a shell with a small elastic thickness of 7 km satisfies the best-fitting between modeled admittance and observation. The density that Crosby (Crosby & McKenzie 2005) used in their study is somewhat larger than the mean value (2550 kg m^{-3}) of the whole highland area. Moreover, the precisions of the gravity and topography they used are lower than those of the GRAIL gravity and topography from LOLA. The difference in elastic thickness between their and our results can be attributed to the difference between the crustal density used in estimation and precision of the gravity and topography data. Considering the well constrained crustal thickness and density around Clavius, the best-fitted elastic thick-

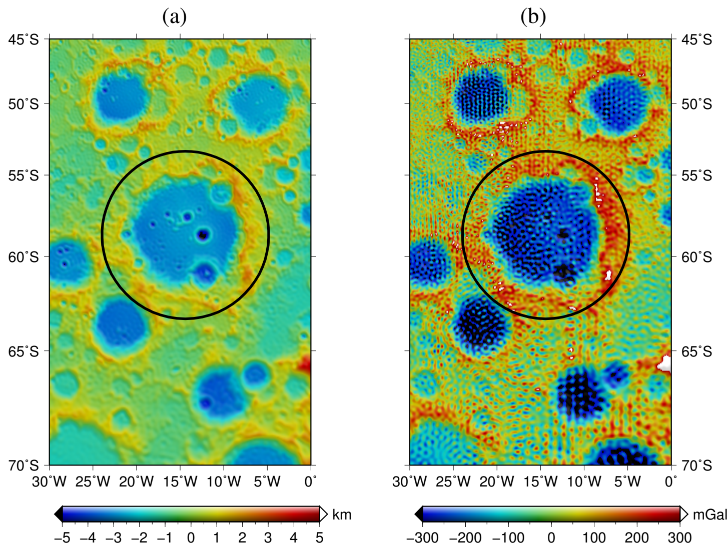

Fig. 1 Mercator projection of topography (a) from LOLA and free air gravity anomaly (b) from GL0990D. Crater Clavius is circled with an angular radius of 5°.

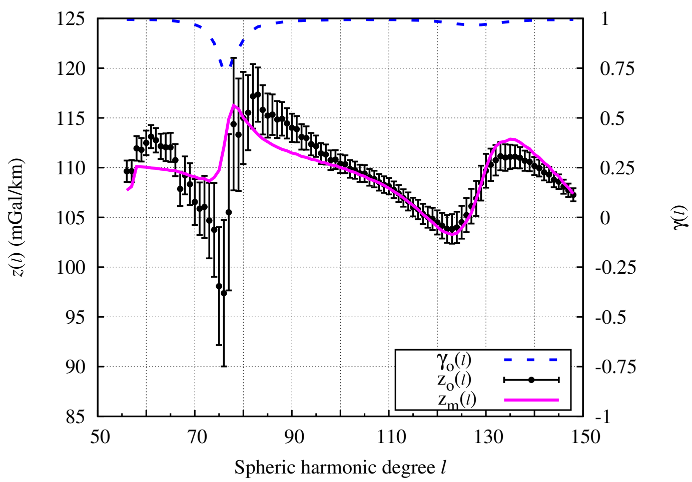

Fig. 2 Correlation spectrum observed (*dashed line*), admittance spectrum observed (error bars) and admittance spectrum modeled (*solid line*) for crater Clavius with a maximum degree of 200.

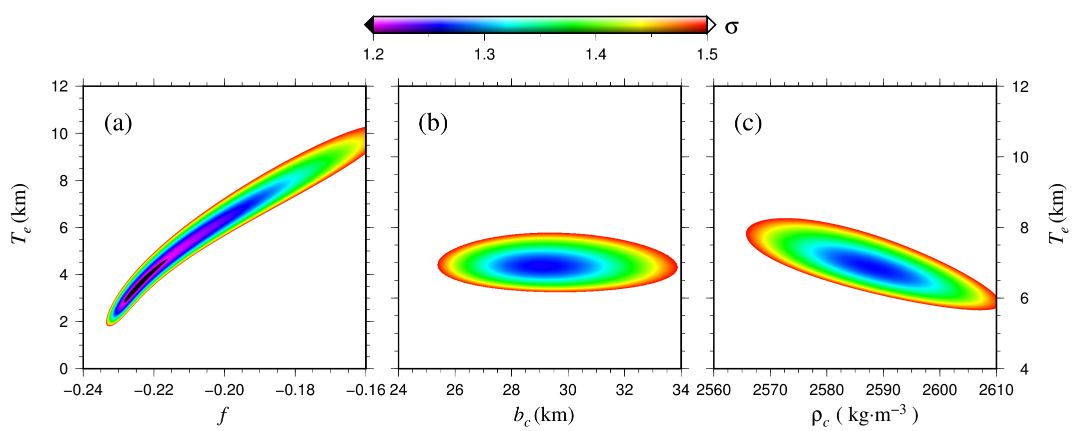

Fig. 3 RMS misfit σ in the trade-off studies between (a) T_e vs. f, (b) T_e vs. b_c and (c) T_e vs. ρ_c.

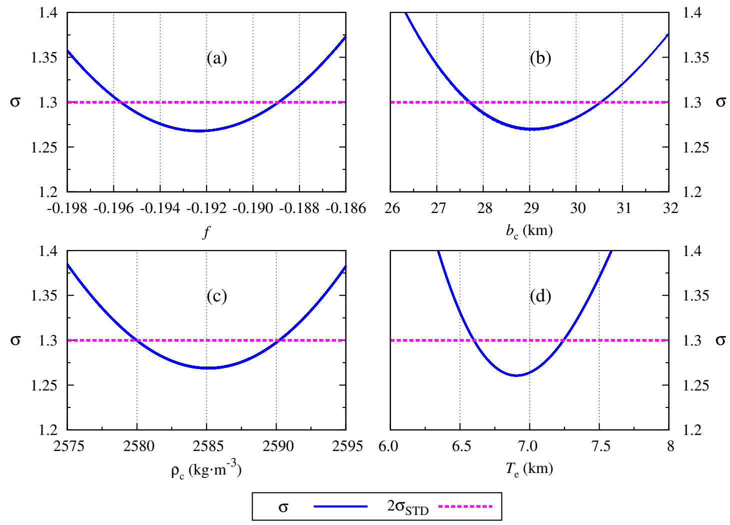

Fig. 4 Minimized misfit σ for the analyzed crater Clavius. Panels (a-d) are σ distributions concerning load ratio f, crustal thickness $b_{\rm c}$, crustal density $\rho_{\rm c}$ and elastic thickness $T_{\rm e}$. Here the *dashed lines* represent $2\sigma_{\rm STD}$.

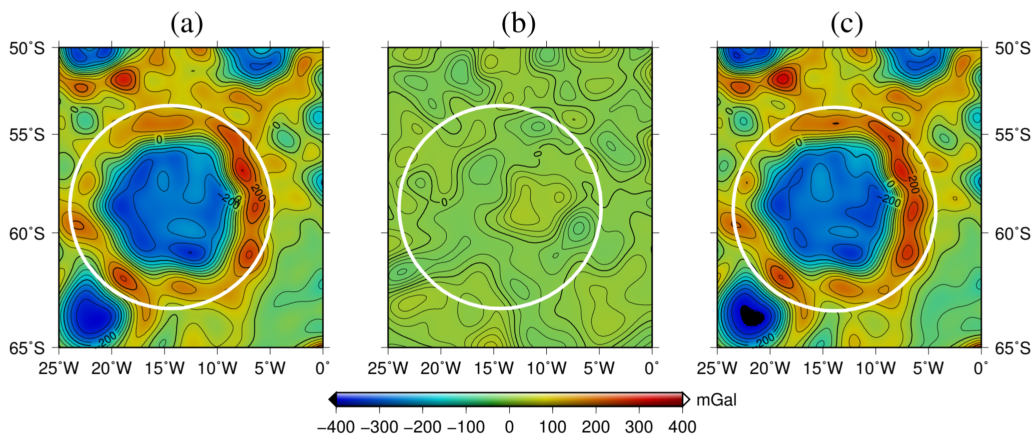

Fig. 5 Localized admittance analysis over crater Clavius (*white circles*). (a) Observed gravity; (b) residual gravity between the modeled gravity and observations; (c) modeled gravity derived with the best-fit parameters.

ness ($\sim$7 km) is rational. Given the best-fitted parameters, we simulate the modeled gravity anomaly based on the four interfaces in Table 2. The modeled gravity anomaly in Figure 5(c) shows a similar feature of the observed free-air gravity anomaly in Figure 5(a). Their difference in Figure 5(b) is found to be around zero mGal. This result indicates that the estimated parameters mentioned above could be an indicator of the subsurface structure beneath Clavius.

4 CONCLUSIONS

In this paper, we employ a PSO to estimate the parameters over crater Clavius. Considering a swarm size of 400 and a maximum number of iterations of 50, we have successfully inversed a best-fitted load ratio f of –0.194. Such a small load ratio agrees with the direct proportion between the uncompensated low-lying topography and its corresponding negative gravity anomaly. It also indicates that a surface load dominates the loads. Constrained within $2\sigma_{\rm STD}$, a small crustal thickness ($\sim$30 km) and a crustal density of $\sim$2587 kg m^{-3} are found in our study, which are quite close to the results from the previous GRAIL research. Considering the well constrained crustal thickness and density around Clavius, the best-fitted elastic thickness ($\sim$7 km) is rational. The spherical shell model was previously proved to be unsatisfactory when using a low-precision gravity field model. Our research indicates that such a model with a small elastic thickness satisfies the best-fitting between modeled admittance and observation. This difference can be attributed to the difference in the crustal density used in estimation and the precision of gravity and topography data. Using the best-estimated parameters, the difference between the modeled gravity anomaly and observations is around zero mGal. These best-estimated parameters could be an indicator of the subsurface structure beneath Clavius.

Acknowledgements The Generic Mapping Tools (GMT) package was used to produce the figures in this paper. Our localized spherical harmonic analyses were performed using the freely available software archive SHTOOLS. This research is supported by a grants from the National Natural Science Foundation of China (Grant Nos. 41864001 and U1831132), Open Fund of State Laboratory of Information Engineering in Surveying, Mapping and Remote Sensing, Wuhan University (Grant No. 17P03) and Guizhou Normal University Doctoral Research Fund. This work is also supported by grants from the Hubei Province Foundation innovation group project (2015CFA011, 2018CFA087), Open Project of Lunar and Planetary Science Laboratory, Macau University of Science and Technology (FDCT 119/2017/A3), and Open Fund of Guizhou Provincial Key Laboratory of Radio Astronomy and Data Processing (KF201813).

Appendix A:

The lithosphere of small celestial bodies shall be modeled as an elastic and thin spherical shell (Turcotte et al. 1981; Zhong & Zuber 2000). The deflection $w_{\rm L}$ (positive downward) of the lithosphere responding to a load q (positive downward) is expressed as (Kraus & Kalnins 1968; Turcotte et al. 1981)

$$\begin{aligned} &D\nabla^6 w_{\rm L} + 4D\nabla^4 w_{\rm L} + ET_{\rm e}R^2\nabla^2 w_{\rm L} + 2ET_{\rm e}R^2 w_{\rm L} \\ &= R^4\left[\left(\nabla^2+2\right)-(1+v)\right] \ , \end{aligned} \tag{A.1}$$

where R is the reference radius of the shell (equivalent to the lunar mean radius), E is Young's modulus, v is Poisson's ratio and D $=ET_{\rm e}^3/[12(1-v^2)]$ is the flexural rigidity (as shown in Table 1). It is known that a geoid displacement is only important for loads whose wavelengths are of the order of the mean radius R (Turcotte et al. 1981). The geoid displacement is thus neglected in the load expression. Then, the load $q_{\rm t}$ induced by a surface load of height $h_{\rm t}$ and corresponding deflection $w_{\rm t}$ of the lithosphere is given by (Turcotte et al. 1981; McGovern et al. 2002)

$$q_{\rm t} = g\left[\rho_{\rm c}h_{\rm t} - (\rho_{\rm m}-\rho_{\rm c})\,w_{\rm t}\right] \ , \tag{A.2}$$

where g is the acceleration at the lunar surface; $\rho_{\rm m}$ and $\rho_{\rm c}$ are mantel and crustal densities listed in Table 1, respectively. Similarly, by neglecting the geoid displacement load $q_{\rm b}$ induced by a subsurface load of height $w_{\rm b}$, the corresponding deflection $h_{\rm b}$ of the lithosphere is expressed as (Turcotte et al. 1981; McGovern et al. 2002)

$$q_{\rm b} = g\left(\rho_{\rm b}w_{\rm b} - \rho_{\rm m}h_{\rm b}\right) \ , \tag{A.3}$$

in which $\rho_{\rm b}$ is the density contrast between the load and its surroundings. Substituting surface and subsurface loads into Equation (A.1) and expanding all the quantities in terms of spherical harmonics, we can have their relationship in the spherical harmonics domain. In the case of surface load, assuming $h_{t,lm}$ and $w_{t,lm}$ are the spherical harmonic coefficients of the surface load height $h_{\rm t}$ and the deflection $w_{\rm t}$ of the lithosphere, their relation is given by (Zhong et al. 2014)

$$w_{t,lm} = C_{s,l}\frac{\Gamma_{s,1}}{\Gamma_{s,2}}h_{t,lm} \ , \tag{A.4}$$

where

$$C_{s,l} = \frac{1}{1+\frac{\Sigma_l+H_l+\mathrm{T}_l}{\Gamma_{s,2}\Theta_l}} \ , \tag{A.5}$$

$$\Gamma_{s,1} = \left(1-\frac{3\rho_{\rm m}}{(2l+1)\,\bar\rho}\right)\frac{\rho_{\rm c}}{\rho_{\rm m}-\rho_{\rm c}} \ , \tag{A.6}$$

$$\Gamma_{s,2} = 1-\frac{3\rho_{\rm m}}{(2l+1)\,\bar\rho}\cdot\left(1-\frac{b_{\rm c}}{R}\right)^{l+2} \ , \tag{A.7}$$

$$\Sigma_l = \sigma(n^3+2n^2) \ , \tag{A.8}$$

$$H_l = -4\sigma\cdot l(l+1) \ , \tag{A.9}$$

$$\mathrm{T}_l = n\cdot\tau \ , \tag{A.10}$$

$$\Theta_l = (n+1+v) \ , \tag{A.11}$$

$$n = l(l+1)-2 \ , \tag{A.12}$$

$$\sigma = \frac{D}{gR^4\left(\rho_{\rm m}-\rho_{\rm c}\right)} \ , \tag{A.13}$$

$$\tau = \frac{ET_{\rm e}}{gR^2\left(\rho_{\rm m}-\rho_{\rm c}\right)} \ . \tag{A.14}$$

As to subsurface load, regarding $w_{b,lm}$ and $h_{b,lm}$ as the spherical harmonic coefficients of the subsurface load height $w_{\rm b}$ and the deflection $h_{\rm b}$ of the lithosphere, their relation is then given by (Zhong et al. 2014)

$$h_{b,lm} = C_{b,l}\frac{\Gamma_{b,1}}{\Gamma_{b,2}}w_{b,lm} \ , \tag{A.15}$$

where

$$C_{b,l} = \frac{1}{1+\frac{\Sigma_l+H_l+\mathrm{T}_l}{\Gamma_{b,2}\Theta_l}} \ , \tag{A.16}$$

$$\Gamma_{b,1} = \frac{\rho_{\rm b}}{\rho_{\rm m}-\rho_{\rm c}} \ , \tag{A.17}$$

$$\Gamma_{b,2} = \frac{\rho_{\rm m}}{\rho_{\rm m}-\rho_{\rm c}} \ . \tag{A.18}$$

Other quantities are similar to those in Equations (A.8)-(A.14). Assuming the initial amplitudes of the surface and subsurface loads are $h_{\rm i}$ and $w_{\rm i}$, respectively, we can have their relations in the forms of their heights and their corresponding lithospherical deflection (Forsyth 1985)

$$h_{\rm i} = h_{\rm t} + w_{\rm t} \ , \tag{A.19}$$

$$w_{\rm i} = w_{\rm b} + h_{\rm b} \ . \tag{A.20}$$

Accordingly, the observed surface topography h represents a sum of the components

$$h = h_{\rm t} - h_{\rm b} \ . \tag{A.21}$$

In order to combine surface and subsurface loads, Forsyth (1985) introduced load ratio f between subsurface and surface loads and it is defined as

$$f = \frac{\rho_{\rm b} w_{\rm i}}{\rho_{\rm c} h_{\rm i}} \ . \tag{A.22}$$

Assuming the estimated parameters are isotropic in the studied area (within angular radius), we can have their relations expressed as spherical harmonic coefficients, which are as follows

$$h_{i,lm} = h_{t,lm} + w_{t,lm} \ , \tag{A.23}$$

$$w_{i,lm} = w_{b,lm} + h_{b,lm} \ , \tag{A.24}$$

$$h_{lm} = h_{t,lm} - h_{b,lm} \ , \tag{A.25}$$

where h_{lm} and $h_{i,lm}$ are the spherical harmonic coefficients of the observed surface height h and its initial height $h_{\rm i}$, respectively. Others have the same meanings. Thus, we can have the relation as

$$h_{i,lm} = \alpha_{t,l} h_{t,lm} \ , \tag{A.26}$$

$$\alpha_{t,l} = 1 + C_{s,l} \frac{\Gamma_{s,1}}{\Gamma_{s,2}} \ , \tag{A.27}$$

$$w_{i,lm} = \alpha_{b,l} w_{b,lm} \ , \tag{A.28}$$

$$\alpha_{b,l} = 1 + C_{b,l} \frac{\Gamma_{b,1}}{\Gamma_{b,2}} \ , \tag{A.29}$$

$$f = -k_l \frac{w_{b,lm}}{h_{t,lm}} \ , \tag{A.30}$$

$$k = \frac{\rho_{\rm b} \alpha_{b,l}}{\rho_{\rm c} \alpha_{t,l}} \ . \tag{A.31}$$

Then, we can deduce the spherical harmonic coefficients $h_{t,lm}$ and $w_{b,lm}$ of the surface load height $h_{\rm t}$ and the subsurface load height $w_{\rm b}$, respectively

$$w_{b,lm} = \frac{h_{lm}}{1 - \frac{k_l}{f} - \alpha_{b,l}} \ , \tag{A.32}$$

$$h_{t,lm} = \frac{h_{lm}}{1 + \frac{f}{k_l}\left(\alpha_{b,l} - 1\right)} \ . \tag{A.33}$$

According to Equations (A.4)–(A.33), the subsurface deflections in Table 2 can be calculated in terms of the spherical harmonic coefficient h_{lm} of the observed surface topography h.

References

Belleguic, V., Lognonné, P., & Wieczorek, M. 2005, Journal of Geophysical Research (Planets), 110, E11005

Bendat, J. S., & Piersol, A. G. 2000, Random Data Analysis and Measurement Procedures (Wiley), 271

Beuthe, M., Le Maistre, S., Rosenblatt, P., Pätzold, M., & Dehant, V. 2012, Journal of Geophysical Research (Planets), 117, E04002

Crosby, A., & McKenzie, D. 2005, Icarus, 173, 100

Forsyth, D. W. 1985, J. Geophys. Res., 90, 12623

Huang, Q., & Wieczorek, M. A. 2012, Journal of Geophysical Research (Planets), 117, E05003

Huang, Q., Xiao, Z., & Xiao, L. 2014, in Lunar and Planetary Science Conference, 45, Lunar and Planetary Science Conference, 1790

Kennedy, J., & Eberhart, R. C. 2001, Swarm Intelligence (Morgan Kaufmann Publishers Inc.), 187

Konopliv, A. S., Park, R. S., Yuan, D.-N., et al. 2014, Geophys. Res. Lett., 41, 1452

Kraus, H., & Kalnins, A. 1968, Journal of Applied Mechanics, 35

McGovern, P. J., Solomon, S. C., Smith, D. E., et al. 2002, Journal of Geophysical Research (Planets), 107, 5136

Park, R. S., Konopliv, A. S., Yuan, D. N., et al. 2015, AGU Fall Meeting Abstracts, G41B

Shi, Y. H. 1998, Proc IEEE Int. conf. on Evolutionary Computation

Smith, D. E., Zuber, M. T., Neumann, G. A., et al. 2010, Geophys. Res. Lett., 37, L18204

Turcotte, D. L., Willemann, R. J., Haxby, W. F., & Norberry, J. 1981, J. Geophys. Res., 86, 3951

Wieczorek, M. A., & Phillips, R. J. 1998, J. Geophys. Res., 103, 1715

Wieczorek, M. A., & Simons, F. J. 2005, Geophysical Journal International, 162, 655

Wieczorek, M. A., & Simons, F. J. 2013, arXiv:1306.3254

Wieczorek, M. A., Neumann, G. A., Nimmo, F., et al. 2013, Science, 339, 671

Zhong, S., & Zuber, M. T. 2000, J. Geophys. Res., 105, 4153

Zhong, Z., Li, F., Yan, J., Yan, P., & Dohm, J. M. 2014, Advances in Space Research, 54, 770

Zhong, Z., Yan, J., Rodriguez, J. A. P., & Dohm, J. M. 2018, Icarus, 309, 411